Chapter

Ultra-Precise MEMS Based Bio-Sensors

Vinayak Pachkawade

Abstract

This chapter evaluated the state-of-the art MEMS sensors used for bio sensing applications. A new class of resonant micro sensor is studied. A sensor structure based on the array of weakly coupled resonators is presented. It is shown that due to the weak coupling employed between the resonators in an array manifest ultra-high sensitivity of the output to the added analytes/biomolecules. Due to the highly-precise output of such bio-sensors, minimum detectable mass in the range of sub-actogram is also possible using such MEMS sensors. Analytical modeling of such micro biosensors is presented in this chapter to understand the key performance parameters. Furthermore, role of these new classes of MEMS resonant biosensors operating at ambient temperature and/or pressure is also discussed.

Keywords: MEMS biosensor, bioelectronics, micro sensors for biological applications, biochemical analyte detection and identification using MEMS

1. Introduction

In recent years, there has been a growing interest in the development and implementation of innovative solutions in the form of a miniaturized bio-sensors. In this regard, in the MEMS community emphasis has been given to design and fabricate highly sensitive, and precise biomass sensors. These bio-sensors are used for detection, identification and measurement of either single and/or multi-analyte/s at lower cost, size, weight, and power consumption. Moreover, resonant devices are widely popular as a sensor for various chemical/biological applications [1]. In the context of biomass sensing, typical examples of resonant sensing include mass identification or detection [2–7]. A key attribute of these sensors is that the output signal is the variation/shift in the resonant frequency (Δf) of a vibrating structure that is subjected to small perturbations in the structural parameters i.e. effective mass/stiffness. Additional features of this method of detection are simple mechanical design, semi-digital nature of the signal (thus using simple frequency measurement system such as frequency counter and not requiring additional analog-to-digital (A/D) conversion circuit), ultra-high resolution [8–10], (up to 10^{-15} grams scale [11–13] and up to 10^{-18} grams scale [14–17]). There are however also a challenge associated with the resonant sensor employing only one resonator; firstly, maximum theoretical frequency shift based parametric sensitivity, $\Delta f/f$ is limited to 1/2 [18]. Sensors of these types are prone to environmental shifts such as pressure and/or temperature. Furthermore, these types of sensors, when used as a mass sensor are able to detect only one type of material (target analyte) at a time thus

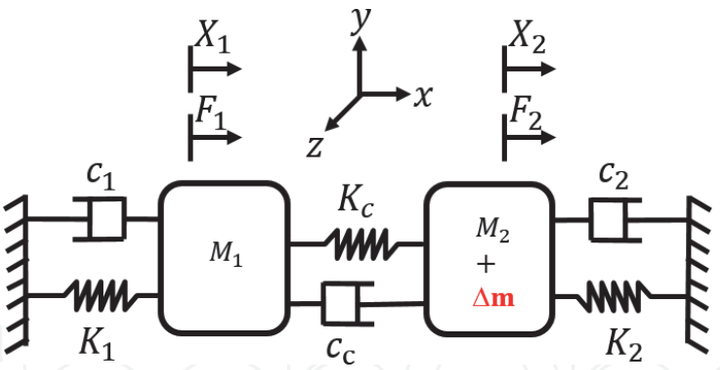

Figure 1.
A schematic representation of a 2-DoF coupled resonant mass-spring-damper system to be used as a high-sensitivity biomass detector/identifier sensor. In a symmetric design, it is assumed that $M_1 = M_2 = M$, $K_1 = K_2 = K$. *A mass perturbation,* Δm *is added onto the mass* M_2*, causing system imbalance, leading to the energy localization/confinement and mode shape change. Mode-shape change is utilized as the output of the sensor.*

avoiding the possibility to rapidly detect and differentiate multiple biochemical analytes in parallel [19].

In the past few years, in the MEMS community, a paradigm shift is observed in the design and implementation of micromechanical resonating sensors. A new perspective is presented in using *1-d* chain of a coupled resonating proof masses, more familiarly refereed as multi degree-of-freedom (m-DoF) array, coupled resonator (CR) array, weakly coupled resonators (WCR) or mode-localized sensors [20–28]. **Figure 1** shows a representative schematic for such system. In this class of a sensors, coupling between the vibrating proof masses is constituted either electrostatically or mechanically. These sensors attribute an ultra-high parametric sensitivity (up to three to four orders high in magnitude) [29]. Such elevated levels of sensitivities are manifested via a novel transduction principle, i.e. sensing magnitude of vibrational energy exchange between the moving proof masses that are subject to a small disruption introduced into the system. This disruption serves to alter an effective mass, Δm of one of the proof mass element in a chain (see **Figure 1**). Primarily, due to relatively higher parametric sensitivities, m-DoF coupled resonators are emerging as an alternative and promising resonant sensing solution.

Other acknowledged advantages of weakly-coupled resonating sensors are linearity (attributed to high sensitivity, relative immunity against responding to common mode noise for example, ambient pressure and/or temperature [30–32] and the parallel detection capability in the context of the mass sensing applications [33–36]. These characteristics make mode-localized coupled resonators effective. For the obvious advantages as given, m-DoF coupled resonant sensors are being pursued over conventional method of resonant sensing, i.e. sensing the frequency shift, Δf of a single resonating device.

2. Theory

A viable method to understand the operation of the mode-localized CR is its analysis through the transfer function model. The transfer function analysis enables to understand the system-level behavior of a biosensor unit. **Figure 1** shows a lumped parameter model of a 2 DoF mass-spring-damper system in the context of CR biosensor. It shows proof masses, M_i, mechanical spring constant, K_i and the damping coefficients, c_i, (i = 1, 2). The c_c models the damping force between the

two resonating proof masses. Two proof masses are coupled through another spring, K_c as shown. A displacement of the proof mass, x_i (i = 1, 2) in response to the applied force, F_i (i = 1, 2) is also indicated. Based on the free body diagram, a set of governing differential equations of motion for 2-DoF mass-spring-damper can be used to derive the theoretical transfer function. Subsequently, an expressions for mode-frequencies, ω_i and modal amplitudes/amplitude ratio (AR) as a function of applied disorder in the mass, δ_m can be obtained.

Following assumptions hold true for a symmetric device- $M_1 = M_2 = M$, $K_1 = K_2 = K$ and $c_1 = c_2 = c$. Forcing vectors F_i acting on the proof masses are the harmonic excitation (drive) forces that cause displacements, x_i, assumed to occur at one frequency. Quantities δ_m and κ are normalized perturbation to the mass and normalized coupling factor, given as $\delta_m = \Delta m/M$ and $\kappa = K_c/K$, respectively. When system experiences imbalance into the initial symmetry *i.e.*, $\Delta m \neq 0$, governing set of equations of motion for the two-coupled proof masses is given as follows:

$$M\ddot{x}_1 + (c + c_c)\dot{x}_1 + (K + K_c)x_1 - c\dot{x}_2 - K_c x_2 = F_1(t) \tag{1}$$

$$(M + \Delta m)\ddot{x}_2 + (c + c_c)\dot{x}_2 + (K + K_c)x_2 - c\dot{x}_1 - K_c x_1 = F_2(t) \tag{2}$$

By operating the system in vacuum, the impact of the following can be reduced, i) damping force of individual proof mass and ii) damping force that occurs between two proof masses, hence $c_1 = c_2 = c_c = 0$ can be assumed for the simplified analysis. Therefore, (1) and (2) can be modified as below:

$$M\ddot{x}_1 + (K + K_c)x_1 - K_c x_2 = F_1(t) \tag{3}$$

$$(M + \Delta m)\ddot{x}_2 + (K + K_c)x_2 - K_c x_1 = F_2(t) \tag{4}$$

By applying a Laplace Transform to Eqs. (3) and (4), following expressions are obtained:

$$G_{11}(s)X_1(s) - G_{12}(s)X_2(s) = F_1(s) \tag{5}$$

$$G_{22}(s)X_2(s) - G_{21}(s)X_1(s) = F_2(s), \tag{6}$$

where

$$G_{11}(s) = s^2M + (K + K_c) \tag{7}$$

$$G_{12}(s) = G_{21}(s) = K_c \tag{8}$$

$$G_{22}(s) = s^2(M + \Delta m) + (K + K_c) \tag{9}$$

In Eq. (6), set $F_2(s) = 0$, and derive an expression for $X_1(s)$ and $X_2(s)$ to use these values back in Eq. (5). An output transfer function is then obtained as follows:

$$G_1(s) = \frac{X_1(s)}{F_1(s)} = \frac{G_{22}(s)}{G_{11}(s)G_{22}(s) - G_{12}(s)G_{21}(s)} \tag{10}$$

$$G_2(s) = \frac{X_2(s)}{F_1(s)} = \frac{G_{21}(s)}{G_{11}(s)G_{22}(s) - G_{12}(s)G_{21}(s)} \tag{11}$$

Similar procedure can be applied to obtain an expression for $G_3(s) = \frac{X_1(s)}{F_2(s)}$ and $G_4(s) = \frac{X_2(s)}{F_2(s)}$. Using the values of $G_{11}(s)$, $G_{12}(s)$ $G_{21}(s)$ and $G_{22}(s)$ derived earlier in Eq. (7) through (9), following equations are obtained

$$G_1(s) = \frac{X_1(s)}{F_1(s)} = \frac{s^2(M+\Delta m)+K_\alpha}{s^4M(M+\Delta m)+s^2K_\alpha[M+(M+\Delta m)]+K_\alpha^2-K_c^2} \tag{12}$$

$$G_2(s) = \frac{X_2(s)}{F_1(s)} = \frac{K_c}{s^4M(M+\Delta m)+s^2K_\alpha[M+(M+\Delta m)]+K_\alpha^2-K_c^2} \tag{13}$$

Here $K_\alpha = (K+K_c)$. Using $s = j\omega$, Eqs. (12) and (13) can be modified to attain

$$G_1(j\omega) = \frac{X_1(j\omega)}{F_1(j\omega)} = \frac{-\omega^2(M+\Delta m)+K_\alpha}{\omega^4M(M+\Delta m)-\omega^2K_\alpha(2M+\Delta m)+K_\alpha^2-K_c^2} \tag{14}$$

$$G_2(j\omega) = \frac{X_2(j\omega)}{F_1(j\omega)} = \frac{K_c}{\omega^4M(M+\Delta m)-\omega^2K_\alpha(2M+\Delta m)+K_\alpha^2-K_c^2} \tag{15}$$

A denominator of Eqs. (14) and (15) is given by

$$\omega^4M(M+\Delta m)-\omega^2K_\alpha(2M+\Delta m)+K_\alpha^2-K_c^2 = 0 \tag{16}$$

Eq. (16) is the characteristic equation of 2 DoF coupled system. Roots of Eq. (16) can be given as

$$\omega_{ip}^2 \approx \frac{K_\alpha(2M+\Delta m)-\sqrt{\Delta m^2K_\alpha^2M^2+4K_c^2\left(M^2+\Delta m\right)}}{2M^2} \tag{17}$$

$$\omega_{op}^2 \approx \frac{K_\alpha(2M+\Delta m)+\sqrt{\Delta m^2K_\alpha^2M^2+4K_c^2\left(M^2+\Delta m\right)}}{2M^2} \tag{18}$$

Here, ω_{ip}^2 and ω_{op}^2 are in-phase and out-of-phase natural mode frequencies of the device. With Δm = 0, Eqs. (17) and (18) take the form $\omega_{ip}^2 = \frac{K}{M}$ and $\omega_{op}^2 = \frac{K+2K_c}{M}$. Dividing (14) by (15), amplitude ratio (AR) is obtained as

$$\frac{H_1(j\omega)}{H_2(j\omega)} = \frac{-\omega^2(M+\Delta m)+K_\alpha}{K_c} \tag{19}$$

By substituting the values of ω in Eq. (19), the expression for mode AR as a function of mass perturbation, Δm is obtained as follows:

$$\frac{H_1(\,j\omega_{ip})}{H_2(\,j\omega_{ip})} = \frac{-\left(\frac{K(2M+\Delta m)-\sqrt{\Delta m^2K_\alpha^2M^2+4K_c^2\left(M^2+\Delta m\right)}}{2M^2}\right)(M+\Delta m)+K_\alpha}{K_c} \tag{20}$$

$$\frac{H_1(\,j\omega_{ip})}{H_2(\,j\omega_{ip})} = \frac{-\left(\frac{K(2M+\Delta m)+\sqrt{\Delta m^2K_\alpha^2M^2+4K_c^2\left(M^2+\Delta m\right)}}{2M^2}\right)(M+\Delta m)+K_\alpha}{K_c} \tag{21}$$

With Δm = 0, Eq. (20) and (21) take the form as

$$\frac{H_1(\,j\omega_{ip})}{H_2(\,j\omega_{ip})} = 1;\ \frac{H_1(\,j\omega_{op})}{H_2(\,j\omega_{op})} = -1 \tag{22}$$

Eq. (22) represents initial balanced condition of a two CR.

2.1 Analytical models

Figure 2 represents the analytical plots of the 2-DoF CR sensor system. In **Figure 2(a)**, mode-frequencies as a function of induced mass disorder is shown. Lower resonant frequency of the out-of-phase mode indicates that a design uses an electrical coupling between the two resonators. With $\delta_m = 0$, two resonant frequencies are closely spaced apart (frequency separation determined by the value of the coupling spring constant, *Kc* used in the system). However, when $\delta_m \neq 0$, resonant mode-frequencies veer away from each other as the magnitude of the δ_m is increased. In **Figure 2(b)**, similar trend can be observed, where, amplitude ratio (AR) as a function of induced mass disorder is shown. Slopes of the curves in each graphs determine the sensitivity of mode-frequencies and AR to the normalized mass perturbation into the system. The theoretical sensitivity norms (in the context of the mass perturbations, Δm) for the amplitude ratio (AR), eigenstate and the resonant frequency used in CR sensors are expressed as below:

$$\left(\frac{x1}{x2}\right)_{ji} = \left|\frac{r_n - r_0}{r_0}\right| \approx \left|\frac{\Delta m}{2K_c}\right| \tag{23}$$

$$(x)_{ji} = \frac{|a_n - a_0|}{|a_0|} \approx \left|\frac{\Delta m}{4K_c}\right| \tag{24}$$

$$\left(f_{ji}\right) = \frac{|f_n - f_0|}{|f_0|} \approx \left|\frac{\Delta m}{2m_{eff}}\right| \tag{25}$$

for j^{th} resonator (j = 1, 2) at i^{th} mode of the frequency response (i = 1, 2), respectively. For the electrostatic coupling between the two resonators, an effective value of the coupling spring is given by $K_c = -(\Delta v^2)\frac{\varepsilon_0 A}{g^3}$, where Δv refers the potential difference between the two masses, g is capacitive gap, ε is permittivity and A is the cross sectional area of the parallel-plate capacitor.

Figure 3 shows a plot of AR variation as a function of mass perturbation. Two different values of coupling spring, K_c are used. For lower effective value of the coupling spring, K_c = 100 N/m, (coupling factor, κ = 0.00075), higher changes in the AR can be extracted (relatively higher slope). This aspect shows the tunable characteristic of a sensitivity in a CR biosensor unit. In **Figure 4**, different forms of the

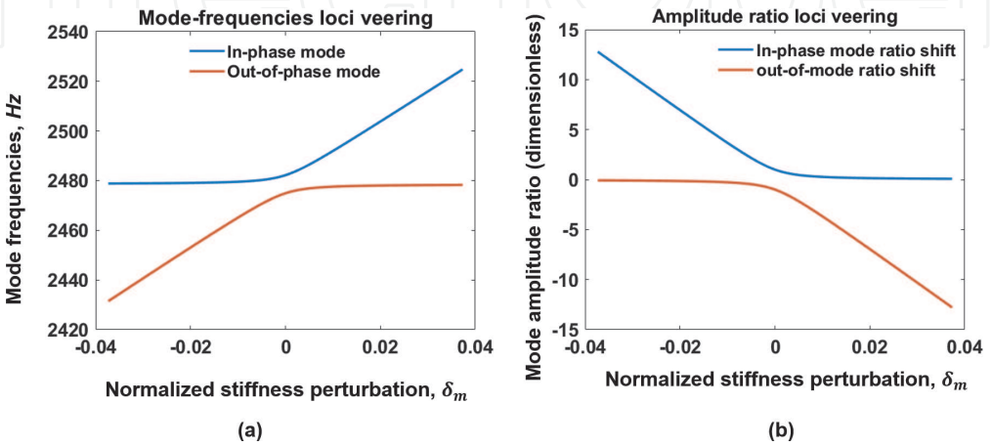

Figure 2.
Mode-frequencies and AR veering phenomenon observed in CR mode-localized mass sensors. δ_m *is the applied normalized mass perturbation. Slope of the AR curves determined the sensitivity. Lower value of the coupling spring,* K_c *enhances sensitivity to the mass perturbation for the AR output.*

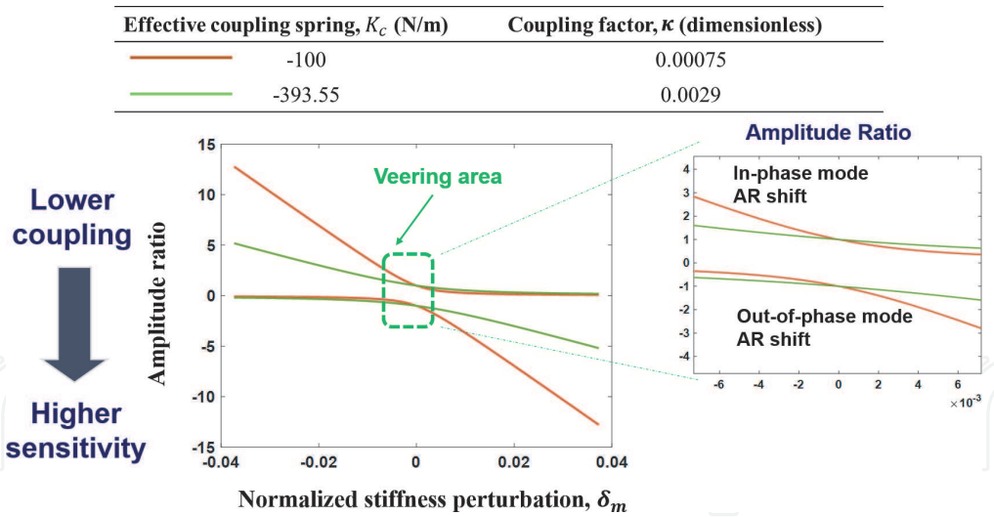

Figure 3.
Amplitude ratio (AR) curve veering in 2-DoF mode-localized coupled resonators mass sensors. The lower coupling factor κ *leads to higher changes in the AR when the normalized perturbation* δ_m *is applied.*

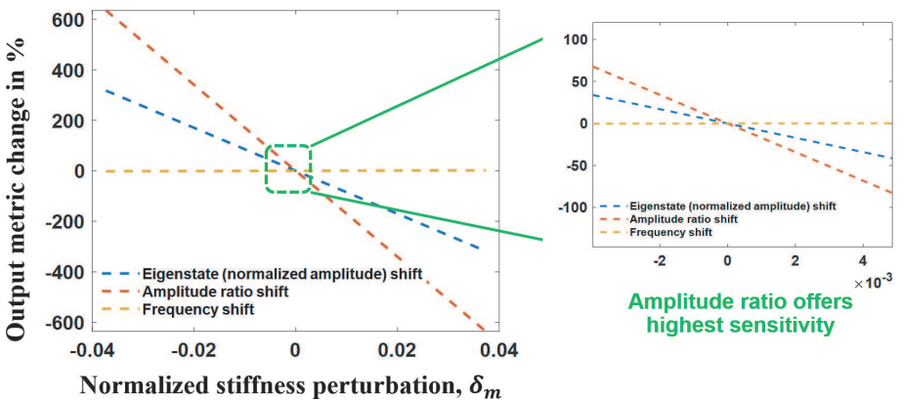

Figure 4.
Different types of the outputs with coupled resonators (CR) sensors. The amplitude ratio (AR) shift shows the highest percentage changes as a function of the mass perturbation, δ_m.

outputs (as expressed in (23) through (25)) are compared against the values of applied mass perturbations in a 2-DoF CR sensor system. As seen, the AR output offers the highest achievable sensitivity. Therefore, AR sensing is the preferred method of the sensing in CR biosensor system. It can be written that $S_{R_i} > S_{a_i} \gg S_{f_i}$. Here, S_{R_i}, $S_{a_{ji}}$ and S_{f_i} denote the *theoretical maximum sensitivity* for AR, amplitude and frequency for j^{th} resonator (j = 1, 2) at the i^{th} mode of the frequency response (i = 1, 2), respectively. Another way to understand the operation of a 2-DoF CR biosensor is through its output frequency response. **Figure 5** shows an output response of resonator 1 and 2 in a 2-DoF coupled resonant (CR) mass biosensor system. As two resonators are used in the CR system, two peaks appear in the output response. Initially, assuming a symmetric system (i.e. $M_1 = M_2 = M$, $K_1 = K_2 = K$), j^{th} resonator (j = 1, 2) vibrate with equal amplitudes at the i^{th} mode (i = 1, 2) of the output response. After the mass disorder, δ_m is introduced, it is observed that vibration amplitudes of the j^{th} resonator (j = 1, 2) at the i^{th} mode (i = 1, 2) of the output response change. An amplitude shift is denoted by Δ_a. The frequency shift, Δf at both the modes is also seen. After the mass perturbation, for the resonator 1, vibration amplitude is seen decreased at the first mode, whereas amplitude is seen increased at the second mode.

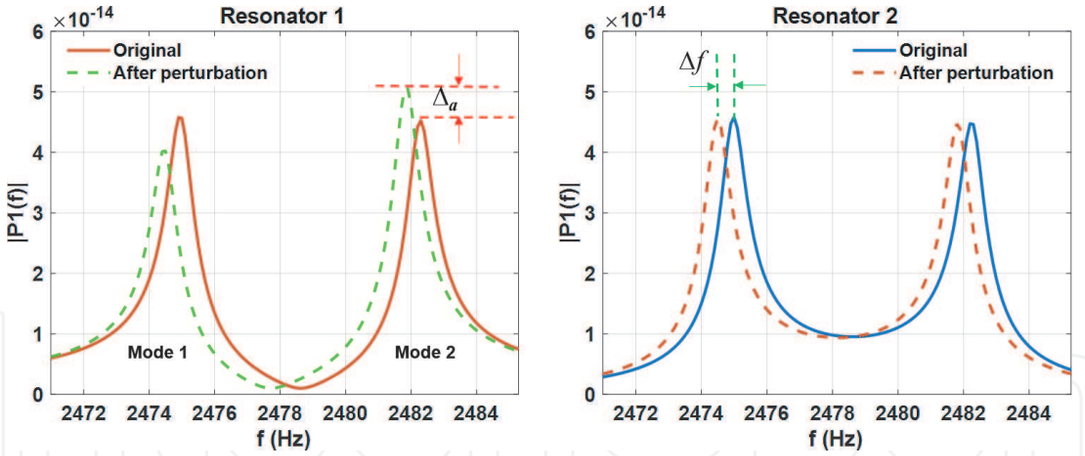

Figure 5.
The output response of a 2-DoF coupled resonator mode-localized design used for biomass sensing applications. Due to the mass addition or removal process, initial eigenmodes and eigen-frequencies of the j^{th} *resonator (*j = 1, 2*) change due to the mode-localization. Changes in the amplitudes,* Δ_a *are found to be 2 to 3 orders high in magnitude than that of the corresponding changes into the frequencies,* Δf *at the* i^{th} *mode (*i = 1, 2*) of the output response.*

2.2 Frequency response and a finite element model (FEM)

Figure 6(a) shows a frequency response (bode diagram) of a 2-DoF CR system. **Figure 6(b)** shows a COMSOL mode shape simulation for a designed geometry of a two mechanically coupled resonators. A structural mechanics module of COMSOL Multiphysics [37] can be used to design CR sensor and simulate for the mode shape

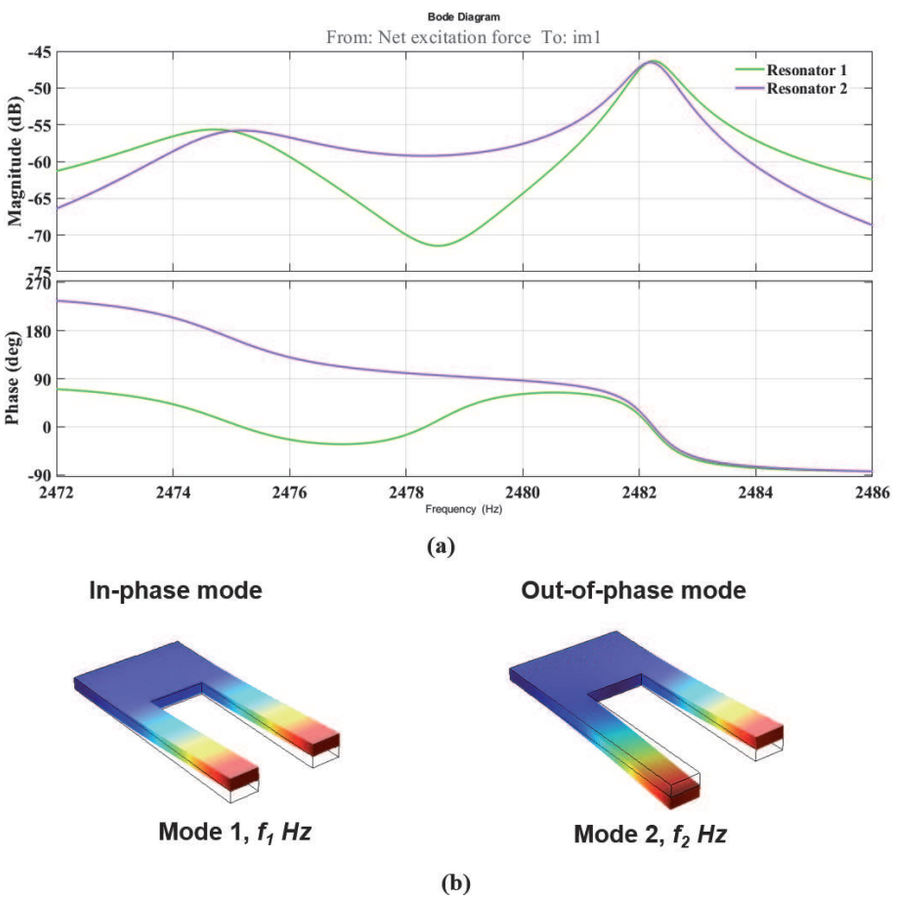

Figure 6.
Output frequency response (bode diagram) of the CR sensor showing the two modes of a 2-DoF sensor. A finite element model is also depicted to determine the mode shape and resonant frequencies of the design. Note the swapping of the two modes as per the coupling used in the sensor.

and eigen-frequencies of the design. As seen from the FEM results, for mode 1, vibrating elements (cantilevers) move in the same direction (in-phase mode) and the same amplitudes [1, 1]. For mode 2, both the cantilevers move in opposite direction (out-of-phase mode) and the same amplitudes [1,-1]. The two simulated mode frequencies are f_1 and f_2 for mode 1 (in-phase) and mode 2 (out-of-phase), respectively. As the FEM illustrates, the coupling used in the design is mechanical. If the coupling used in the design is electrical, out-of-phase mode precedes the in-phase mode as seen in the bode diagram (note the phase difference of the two resonators).

3. Case studies in m-DoF resonant mass sensing

In this section, different types of MEMS ultra-precise sensors based on the m-DoF CR architecture are discussed. In MEMS resonant biosensors, a surface of the micromechanical resonator is coated with a sensitive thin film. A resonant frequency shift is monitored as a result of adsorption/absorption of the target analyte/s [19]. In the same framework, CR structures are used as a mass sensors owing to the enhanced mass sensitivity and parallel monitoring of multiple analyte/s.

3.1 Study I

For the first time, it was proposed that a vibration mode localization can be used to demonstrate an elevated mass sensitivity [36]. A fabricated prototype is shown in **Figure 7(a)**. In this work, two nearly identical mechanically coupled gold-foil microcantilevers were used. For the experimentation, borosilicate microspheres (mean diameter of 4.9 μm with a mass of ≈154 pg were added on cantilever 2. Piezoelectric shaker was used for the driving scheme for the sensor. A laser doppler vibrometer was used to capture the tip velocities at different locations of individual cantilevers. An output plot as seen in **Figure 7(b)** was obtained to show eigenstate variation as a function of normalized mass perturbation, δ_m. With $\Delta m = 0$, vibration amplitudes of cantilevers 1 and 2 at two mode frequencies (i.e. two distinct modes as in-phase and out-of-phase) are seen. Uneven amplitudes for both the cantilevers at both the modes are result of fabrication mismatch. With $\Delta m \neq 0$, vibration amplitudes of both the cantilevers change at both the modes. With mass added to cantilever 2, amplitudes of both the resonators at both the modes are seen to be increased. Amplitude of resonator 1 is relatively higher than amplitude of resonator 2 at the first mode (at lower frequency in the response). Amplitude of resonator 2 is relatively higher than amplitude of resonator 1 at the second mode (at the higher frequency in the response). A relatively larger shift (either in amplitude or resonant frequency) indicates vibration energy is localized to that particular cantilever at the mode of operation. With a mass differential (Δm) in the system, resonant frequencies of both the cantilevers at both the modes also change. However, relative changes in the amplitudes are orders of magnitude higher than the changes in frequencies. This work experimentally demonstrated about two orders higher in magnitude relative changes into the eigenstates (5–7%) than relative changes in the frequencies (0.01%). Enhanced sensitivity of eigenstates to the added mass was attributed to the decreased scaled coupling strength, κ between the two cantilevers. Each eigenstate is the normalized vector formed by the amplitudes of the two vibrating elements (cantilevers) at a corresponding resonance frequency. In the same work, mass removal from the cantilever surface resulted in return of eigenstates to their original values.

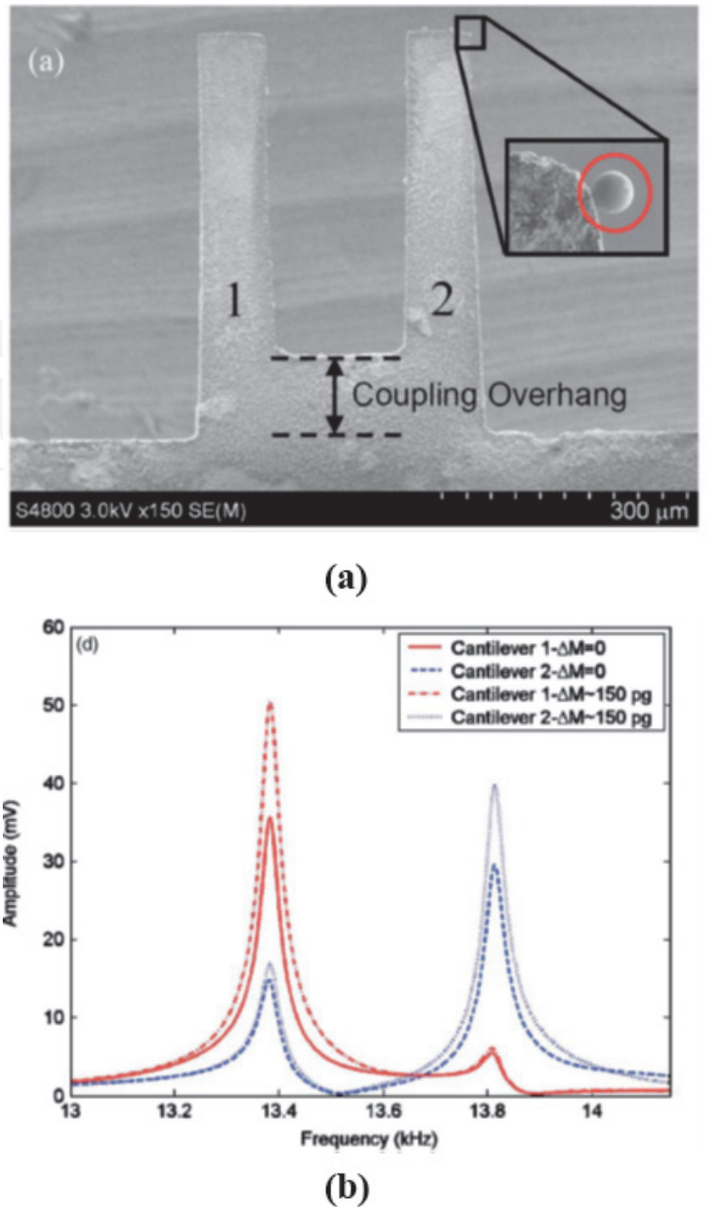

Figure 7.
Ultrasensitive mass sensor using a mode localization in coupled microcantilevers (a) fabricated prototype and (b) amplitude-frequency response of a fabricated prototype before and after the mass imbalance introduced into the system [33]. Reprinted from [33] with the permission of AIP Publishing.

3.2 Study II

Moreover, using an array of polysilicon microcantilevers (up to 15) it is possible to record up to 3 orders higher changes in eigenstate based output of the sensor [35]. In an array of cantilevers, each pattern of eigenmode shifts is unique. Therefore, by examining an experimentally measured pattern of eigenmode shifts it is possible to determine to which cantilever a target analyte particle has adhered. A mass sensitivity of up to two orders higher was found as opposed to the previous work [36] reported by the same group. A mass sensitivity of up to three orders higher was found as opposed to relative frequency shifts. It is therefore feasible to design coupled resonant (CR) microstructures and use eigenmode as an output metric for enhanced parametric sensitivity over resonant sensors that use frequency shift output. However, it is also evident that merely adding the number of resonators in a 1-dimensional (1-*d*) chain does not necessarily increase the parametric sensitivity in proportion.

3.3 Study III

In a study, an array of four micro beams, S_1-S_4 are attached to a common shuttle mass, SM for the detection and identification of multiple analytes [19, 38]. Geometrical asymmetry in the micro beams (length mismatch) assured sufficient separation of individual resonant peaks (as seen in **Figure 8(a)**) at the corresponding eigenmode frequencies in the output response. An output response of the fabricated prototype along with mode shapes are shown in **Figure 8(a)**. A capillary tube containing the specific polymer solutions was interfaced to one or all of the micro beams to functionalize them for vapor detection. Specifically, toluene and methanol, and toluene/methanol mixtures were used with the polymers to prepare analyte concentration for the functionalization of the surface of the microbeam/s in an

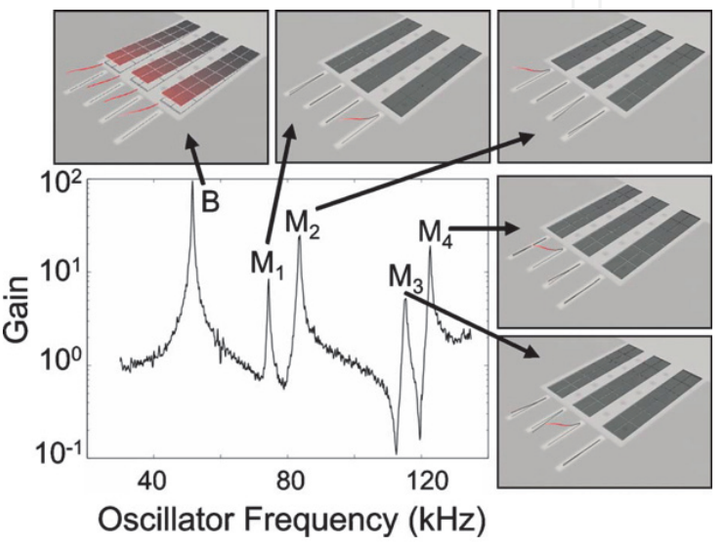

(a)

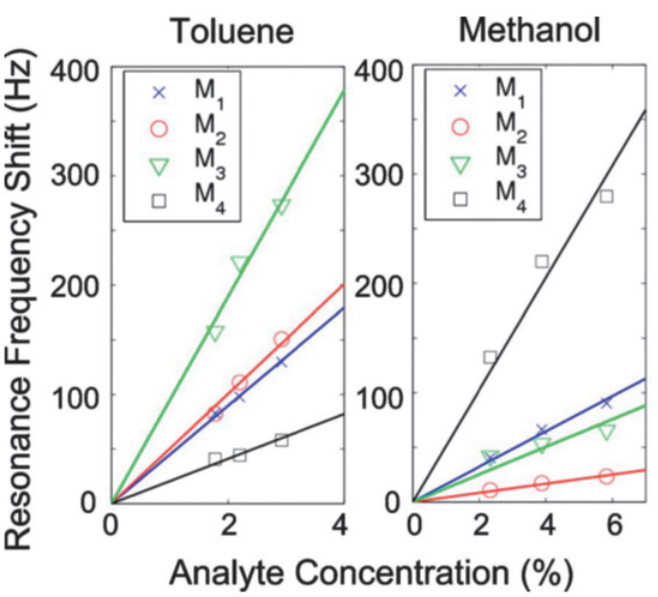

(b)

Figure 8.
Frequency response of the single input single output scheme in an array of coupled micro beams. (a) Composite response indicated by B and the individual mode-frequencies (M1-M4) of the mode-localized micro beams upon mass absorption due to the added analyte concentration. Also shown are the resonant mode shapes of the system. (b) Resonant frequency shifts of the four individual modes as a function of added mass concentration of the analyte. Slopes of the curve determine the sensitivity to the analyte, also making it possible to identify particular vapor concentration. Reprinted from [38] with the permission of AIP Publishing.

array. The functionalized prototype was excited to motion by the piezoelectric actuator operating at a pressure level of 200 *Torr*. As shown in **Figure 8(b)**, a single output signal (resonant frequency shifts of all micro beams as a function of analyte concentration in %) was measured optically from the SM to obtain the composite response due to the mode-localization. Detection process is as follows: i) measure the resonance frequencies, M1-M4 (without added mass) in the pure nitrogen gas, ii) introduce an analyte and wait for the absorption to reach steady state, iii) measure the resonance frequencies once more, and determining the resulting frequency shifts. In this experiment, the frequency shift of each localized microbeam mode (M1-M4) was determined for various analyte concentrations (**Figure 8(b)**). As observed from **Figure 8(b)**, M3 shows the highest sensitivity to the toluene, whereas, M4 exhibits highest sensitivity to the added mass concentration of the methanol. Knowing the shifts of the two most sensitive microbeam modes M3 and M4 and their sensitivities from **Figure 8(b)**, the concentrations of methanol and toluene in the vapor were estimated to be 2.8% and 2.0%, respectively, and found in good agreement with the actual concentrations of 2.3% methanol and 2.3% toluene.

3.4 Study IV

In the recent study, 'Fano resonances' were observed in purely mechanical systems constituted by an array of nano and microcantilever resonators [39]. An array of micro/nano-scale cantilevers were used for mass sensing. A fabricated prototype and the output response is shown in **Figure 9**. Nanoscale cantilevers (thickness of 100 *nm*) fabricated of silicon nitrate were excited with piezoelectric disk shaker. A laser optical based detection was performed with sub-picometer resolution. Cantilevers here are directly connected to the bulk silicon without any suspended overhang at the base. As a consequence, each cantilever resonance is said to be identified by the main resonance curve (Lorentzian curve). No other resonant peak (entangled states due to coupling) are observed in the output response. Instead, due to an interference between the tails of the Lorentzian curve and the resonance peaks of the other cantilevers in an array, it was said that fano-peaks appeared at the corresponding resonant frequencies of the other cantilevers in an array (**Figure 9(b)**). Increased sensitivity (i.e. being able to measure smallest change in mass, Δm of up to 5 *pg*, $\Delta m \quad m/Q$) of fano-resonances was attributed to their exhibited relatively higher quality factor, Q (10× than the main resonance

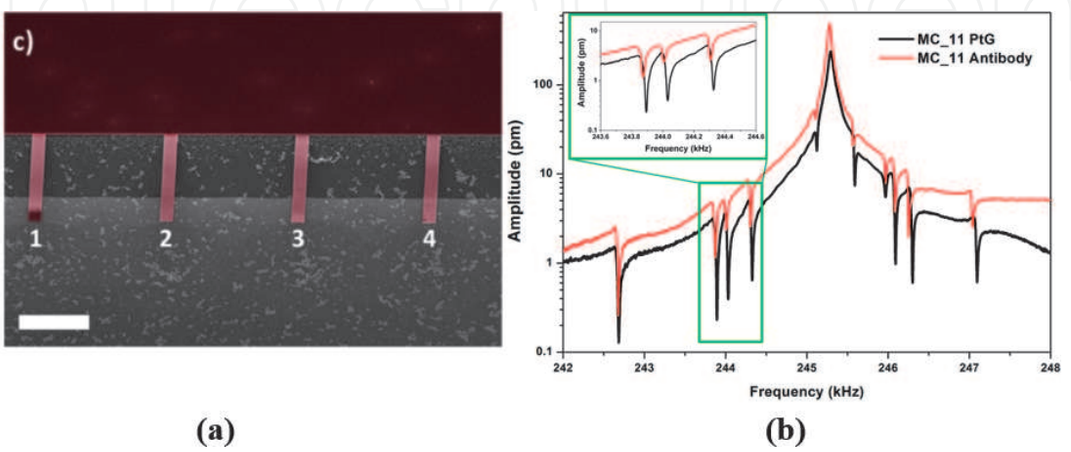

Figure 9.
Fabricated prototype (a) and (b) vibration spectra of one cantilever in an array. Up to 9 cantilevers, not shown here were used in this work to propose a single and fast measurement scheme for cantilever arrays using Fano-resonance analysis [39]. Reprinted from [39] with the permission of Springer Nature under creative commons licenses.

peak). A negative shift in the resonant frequencies of all the 'Fano-resonances' was observed as the results of parallel mass loading on all the cantilevers in an array. Therefore, a single, fast measurement scheme (parallelization) was proposed to characterize the frequency response of one cantilever in an array. Several configurations of micro/nano scale cantilever arrays were fabricated and experimental results were given along with the theory model.

4. Common-mode-rejection in resonant mass sensors

Mode-localized sensors that utilize an array of ideally identical, weakly coupled, vibrating microstructural elements are shown to be relatively immune to the false output. Environmental factors (such as ambient pressure [30, 32], temperature [31, 40]) and/or nonspecific bindings (in case of mass sensing) influence all the vibrating elements uniformly. These factors as mentioned ideally does not affect the eigenmodes of the system, while shifts in the resonance frequencies still occur. One of the early work addressing the common-mode rejection of mode-localized sensor is given in [30]. As shown in **Figure 1**, in a 2-DoF WCR sensor, induced mismatch (Δm) affects one of the resonator. This is called a mass differential mode of operation. However, environmental variable such as temperature or pressure affects both the resonators simultaneously, which is termed as common-mode behavior of the micromechanical mode-localized sensors. It is found that, the mode-localized sensor is efficient in rejecting a common-mode noise (temperature and pressure) to the first order.

Table 1 provides a comparative performance summary (in terms of the attainable mass sensitivity and minimum detectable mass) of the ultra-precise and highly sensitive resonant mass sensors.

Reference	Output used	Relative sensitivity [a]	Minimum detectable mass, Δm	DoF	Material used
[36]	eigenstates	5% to 7% (higher than frequency shift output)	154 *pg*	2	borosilicate microspheres
[26]	eigenstates	3 orders higher	13.5 *pg*	2	platinum patches
[19, 38]	Frequency shift	NA	NA	4	polymer solutions
[41]	Frequency shift	NA	1.42×10^{-14} *kg*	3	NA
[42]	eigenstates	7000	10 *pg*	3	polystyrene micro-spheres
[39]	Frequency shift	NA	5 *pg*	4	NA
[43]	AR	34,361	2.1 *ng*	2	NA
[24]	AR	2.5%/*pg* (estimated via numerical model)	6 *pg*	2	NA
[44]	AR (Atmospheric pressure test)	25.31 (two orders higher than frequency shift output)	180 *ng*	3	Nanoparticles used
[34]	Eigenstates/ frequency shifts	NA	NA	4	Thermally killed bacteria

[a] *Relative sensitivity is the ratio of sensitivity of eigenstate/s or AR output to the sensitivity of frequency shift output.*

Table 1.
Mode-localized mass sensors summary.

5. Conclusion

In this chapter, the state-of-the-art in MEMS resonant sensor is studied. Numerical models were presented to understand the operation of the ultra-precise, high sensitivity devices used for the bio applications. Key performance parameters such as mass sensitivity was derived for the different available outputs in the CR resonant mass sensors. From the recent case studies and a comparative analysis as provided in **Table 1**, it can be concluded that CR resonant biosensor is emerging as a new sensing standard in the MEMS community.

Abbreviations and nomenclature

MEMS	Micro-electromechnical systems
m-DoF	multi-degree of freedom
CR	Coupled resonators
WCR	Weakly coupled resonators
A/D	Analog-to-digital converter
AR	Amplitude ratio
M_i	Proof mass *gram*
K_i	Mechanical spring constant *N/m*
c_i	Damping *Ns/m*
F	Forcing term *N*
x	Displacement of the proof mass *m*
K_c	Coupling spring constant (electrical) *N/m*
κ	Coupling factor *Unitless*
Δm	Mass perturbation *gram*
δ	Normalized perturbation *Unitless*
δ_m	Normalized mass perturbation *Unitless*
ω_{ip}	In-phase mode frequency *rad/sec*
ω_{op}	Out-of-phase mode frequency *rad/sec*
$\left(\frac{x1}{x2}\right)_{ji}$	Amplitude ratio of the j^{th} resonator at the i^{th} mode of the frequency response *Unitless*
$(x)_{ji}$	Amplitude of the j^{th} resonator at the i^{th} mode of the frequency response *V*
$\left(f_{ji}\right)$	Resonant frequency of the j^{th} resonator at the i^{th} mode of the frequency response *Hz*
Δf	Frequency shift *Hz*
Δ_a	Amplitude shift *V*
$\Delta f/f$	Frequency shift (normalized) *Unitless*
S_{R_i}	Sensitivity of AR shift to the normalized mass perturbation $V/V/\delta_m$
$S_{a_{ji}}$	Sensitivity of amplitude shift to the normalized mass perturbation V/δ_m
S_{f_i}	Sensitivity of frequency shift to the normalized mass perturbation Hz/δ_m

Author details

Vinayak Pachkawade
University of Liege, Belgium

*Address all correspondence to: vpachkawade@uliege.be

IntechOpen

References

[1] Wasisto HS, Merzsch S, Waag A, Uhde E, Salthammer T, Peiner E. Airborne engineered nanoparticle mass sensor based on a silicon resonant cantilever. Sensors Actuators, B Chem. 2013;

[2] Zhang H, Kim ES. Micromachined acoustic resonant mass sensor. J Microelectromechanical Syst. 2005;

[3] Burg TP, Mirza AR, Milovic N, Tsau CH, Popescu GA, Foster JS, et al. Vacuum-packaged suspended microchannel resonant mass sensor for biomolecular detection. J Microelectromechanical Syst. 2006;

[4] Zhang W, Baskaran R, Turner KL. Effect of cubic nonlinearity on auto-parametrically amplified resonant MEMS mass sensor. Sensors Actuators, A Phys. 2002;

[5] Park K, Kim N, Morisette DT, Aluru NR, Bashir R. Resonant MEMS mass sensors for measurement of microdroplet evaporation. J Microelectromechanical Syst. 2012;

[6] Lee JEY, Bahreyni B, Zhu Y, Seshia AA. Ultrasensitive mass balance based on a bulk acoustic mode single-crystal silicon resonator. Appl Phys Lett. 2007;

[7] Li L. Simulation of Mass Sensor Based on Luminescence of Micro/Nano Electromechanical Resonator. IEEE Electron Device Lett. 2017;

[8] Jin D, Liu J, Li X, Liu M, Zuo G, Wang Y, et al. Tens femtogram resoluble piezoresistive cantilever sensors with optimized high-mode resonance excitation. In: Proceedings of 1st IEEE International Conference on Nano Micro Engineered and Molecular Systems, 1st IEEE-NEMS. 2006.

[9] Zou X, Thiruvenkatanathan P, Seshia AA. A high-resolution micro-electro-mechanical resonant tilt sensor. Sensors Actuators, A Phys. 2014;

[10] Zou X, Thiruvenkatanathan P, Seshia AA. Micro-electro-mechanical resonant tilt sensor with 250 nano-radian resolution. In: 2013 Joint European Frequency and Time Forum and International Frequency Control Symposium, EFTF/IFC 2013. 2013.

[11] Gupta A, Akin D, Bashir R. Single virus particle mass detection using microresonators with nanoscale thickness. Appl Phys Lett. 2004;

[12] Sone H, Okano H, Hosaka S. Picogram mass sensor using piezoresistive cantilever for biosensor. In: Japanese Journal of Applied Physics, Part 1: Regular Papers and Short Notes and Review Papers. 2004.

[13] Ilic B, Czaplewski D, Zalalutdinov M, Craighead HG, Neuzil P, Campagnolo C, et al. Single cell detection with micromechanical oscillators. J Vac Sci Technol B Microelectron Nanom Struct. 2001;

[14] Baek IB, Byun S, Lee BK, Ryu JH, Kim Y, Yoon YS, et al. Attogram mass sensing based on silicon microbeam resonators. Sci Rep. 2017;

[15] Davis ZJ, Boisen A. Aluminum nanocantilevers for high sensitivity mass sensors. Appl Phys Lett. 2005;

[16] Ekinci KL, Huang XMH, Roukes ML. Ultrasensitive nanoelectromechanical mass detection. Appl Phys Lett. 2004;

[17] Ono T, Esashi M. Magnetic force and optical force sensing with ultrathin silicon resonator. Rev Sci Instrum. 2003;

[18] Giessibl FJ. A direct method to calculate tip-sample forces from frequency shifts in frequency-modulation

atomic force microscopy. Appl Phys Lett. 2001;

[19] DeMartini BE, Rhoads JF, Shaw SW, Turner KL. A single input-single output mass sensor based on a coupled array of microresonators. Sensors Actuators, A Phys. 2007;

[20] Li L, Zhang YP, Ma CC, Liu CC, Peng B. Anti-symmetric mode vibration of electrostatically actuated clamped-clamped microbeams for mass sensing. Micromachines. 2020;

[21] Liang J, Hao Y, Kang H, Ruan B, Chang H. A Mode-Localized Voltmeter with Resolution of 46.8 Nanovolts. In: 2019 20th International Conference on Solid-State Sensors, Actuators and Microsystems and Eurosensors XXXIII, TRANSDUCERS 2019 and EUROSENSORS XXXIII. 2019.

[22] Manav M, Srikantha Phani A, Cretu E. Mode Localization and Sensitivity in Weakly Coupled Resonators. IEEE Sens J. 2019;

[23] Pandit M, Zhao C, Sobreviela G, Du S, Zou X, Seshia A. Utilizing energy localization in weakly coupled nonlinear resonators for sensing applications. J Microelectromechanical Syst. 2019;

[24] Rabenimanana T, Walter V, Kacem N, Le Moal P, Bourbon G, Lardiès J. Mass sensor using mode localization in two weakly coupled MEMS cantilevers with different lengths: Design and experimental model validation. Sensors Actuators, A Phys. 2019;

[25] Tao G, Choubey B. A simple technique to readout and characterize coupled MEMS resonators. J Microelectromechanical Syst. 2016;

[26] Thiruvenkatanathan P, Yan J, Woodhouse J, Aziz A, Seshia AA. Ultrasensitive mode-localized mass sensor with electrically tunable parametric sensitivity. Applied Physics Letters. 2010.

[27] Venstra WJ, Van Leeuwen R, Van Der Zant HSJ. Strongly coupled modes in a weakly driven micromechanical resonator. Appl Phys Lett. 2012 Dec 10; 101(24).

[28] Zhang H, Chang H, Yuan W. Characterization of forced localization of disordered weakly coupled micromechanical resonators. Microsystems Nanoeng. 2017;

[29] Zhao C, Wood GS, Xie J, Chang H, Pu SH, Kraft M. A Three Degree-of-Freedom Weakly Coupled Resonator Sensor with Enhanced Stiffness Sensitivity. J Microelectromechanical Syst. 2016;

[30] Thiruvenkatanathan P, Yan J, Seshia AA. Common mode rejection in electrically coupled MEMS resonators utilizing mode localization for sensor applications. In: 2009 IEEE International Frequency Control Symposium Joint with the 22nd European Frequency and Time Forum. 2009.

[31] Zhong J, Yang J, Chang H. The temperature drift suppression of mode-localized resonant sensors. In: Proceedings of the IEEE International Conference on Micro Electro Mechanical Systems (MEMS). 2018.

[32] Zhang H, Zhong J, Yuan W, Yang J, Chang H. Ambient pressure drift rejection of mode-localized resonant sensors. In: Proceedings of the IEEE International Conference on Micro Electro Mechanical Systems (MEMS). 2017.

[33] Chellasivalingam M, Pandit M, Kalberer M, Seshia AA. Ultra-fine Particulate Detection using Mode-localized MEMS Resonators. In: IFCS/EFTF 2019 - Joint Conference of the IEEE International Frequency Control Symposium and European Frequency and Time Forum, Proceedings. 2019.

[34] Marquez S, Alvarez M, Plaza JA, Villanueva LG, Dominguez C, Lechuga

LM. Asymmetrically coupled resonators for mass sensing. Appl Phys Lett. 2017;

[35] Spletzer M, Raman A, Sumali H, Sullivan JP. Highly sensitive mass detection and identification using vibration localization in coupled microcantilever arrays. Appl Phys Lett. 2008;

[36] Spletzer M, Raman A, Wu AQ, Xu X, Reifenberger R. Ultrasensitive mass sensing using mode localization in coupled microcantilevers. Appl Phys Lett. 2006;

[37] COMSOL. COMSOL Multiphysics® Modeling Software. Comsol. 2016;

[38] DeMartini BE, Rhoads JF, Zielke MA, Owen KG, Shaw SW, Turner KL. A single input-single output coupled microresonator array for the detection and identification of multiple analytes. Appl Phys Lett. 2008;

[39] Stassi S, Chiadò A, Calafiore G, Palmara G, Cabrini S, Ricciardi C. Experimental evidence of Fano resonances in nanomechanical resonators. Sci Rep. 2017;

[40] Pandit M, Zhao C, Sobreviela G, Seshia AA. Immunity to Temperature Fluctuations in Weakly Coupled MEMS Resonators. In: Proceedings of IEEE Sensors. 2018.

[41] Hajhashemi MS, Bahreyni B. Characterization of disturbances in systems of coupled micro-resonator arrays. IEEE Sens J. 2012;

[42] Wang DF, Li X, Yang X, Ikehara T, Maeda R. Enhancing amplitude changes by mode localization in trio cantilevers with mass perturbation. J Micromechanics Microengineering. 2015;

[43] Wood GS, Zhao C, Pu SH, Boden SA, Sari I, Kraft M. Mass sensor utilising the mode-localisation effect in an electrostatically-coupled MEMS resonator pair fabricated using an SOI process. Microelectron Eng. 2016;

[44] Wang Y, Zhao C, Wang C, Cerica D, Baijot M, Xiao Q, et al. A mass sensor based on 3-DOF mode localized coupled resonator under atmospheric pressure. Sensors Actuators, A Phys [Internet]. 2018;279(June):254–62. Available from: https://doi.org/10.1016/j.sna.2018.06.028